GFZ

Helmholtz-Zentrum
POTSDAM

RESEARCH ARTICLE

Key Points:
- We investigate limits on detection/ analysis of small earthquakes using synthetic seismograms subjected to various path/sensor effects
- Moment magnitude, stress drop, source-receiver distance, attenuation, and sensor properties are crucial for earthquake detection
- S-to-P amplitude ratios decrease with decreasing magnitudes due to different attenuation of P and S waves

Supporting Information:
- Supporting Information S1
- Table S1
- Figures S1–S69

Correspondence to:
G. Kwiatek,
kwiatek@gfz-potsdam.de

# Theoretical limits on detection and analysis of small earthquakes

Grzegorz Kwiatek[1] and Yehuda Ben-Zion[2]

[1]Section 4.2: Geomechanics and Rheology, Helmholtz Centre Potsdam, GFZ German Research Centre for Geosciences, Potsdam, Germany, [2]Department of Earth Sciences, University of Southern California, Los Angeles, California, USA

Abstract We investigate theoretical limits on detection and reliable estimates of source characteristics of small earthquakes using synthetic seismograms for shear/tensile dislocations on kinematic circular ruptures and observed seismic noise and properties of several acquisition systems (instrument response, sampling rate). Simulated source time functions for shear/tensile dislocation events with different magnitudes, static stress drops, and rupture velocities provide estimates for the amplitude and frequency content of P and S phases at various observation angles. The source time functions are convolved with a Green's function for a homogenous solid assuming given P, S wave velocities and attenuation coefficients and a given instrument response. The synthetic waveforms are superposed with average levels of the observed ambient seismic noise up to 1 kHz. The combined seismograms are used to calculate signal-to-noise ratios and expected frequency content of P and S phases at various locations. The synthetic simulations of signal-to-noise ratio reproduce observed ratios extracted from several well-recorded data sets. The results provide guidelines on detection of small events in various geological environments, along with information relevant to reliable analyses of earthquake source properties.

1. Introduction

Recent increase in the number and spatial density of seismometers at regional and local scales [e.g., *Okada et al.*, 2004; *Lin et al.*, 2013], coupled with improved sensors and processing techniques, provide unprecedented opportunities for detecting and analyzing source properties of smaller events. This can increase the monitoring resolution and improve understanding on earthquake physics in natural and human-related activities (e.g., reservoirs, geothermal and oil production, and mines). High-quality regional seismic networks such as those in Japan, Taiwan, and parts of the U.S. routinely detect events with moment magnitude M_W close to zero [e.g., *Hauksson et al.*, 2012]. Spatially dense array data recorded by surface sensors allow for detection and possible analysis of source characteristics of subzero events [e.g., *Ben-Zion et al.*, 2015; *Inbal et al.*, 2015]. In special situations involving deep mines or borehole arrays, with seismic sensors in 3-D volumes around target events, earthquakes with $M_W < -4.0$ involving seismic sources of <1 dm size are detected and analyzed [*Kwiatek et al.*, 2010, 2011; *Plenkers et al.*, 2010].

Clarifying the theoretical limits on event detection and reliable analysis of earthquake source properties is important for multiple reasons. Such knowledge can help in optimizing the design of seismic networks for different purposes. It can also help in assessing whether reports on event detection and derived source properties are consistent with expected propagation of information from sources to receivers. This can contribute to several topics of ongoing debate, such as whether reported deviations of earthquake properties from self-similarity may be genuine or are consequences of observational limitations [e.g., *Ide et al.*, 2003; *Kwiatek et al.*, 2011]. Another important issue is the possibility of providing observational evidence for a minimum earthquake size related to frictional sliding [e.g., *Dieterich*, 1992; *Ben-Zion*, 2003], given detection limitations. A related topic is whether conflicting reports on precursory seismic activity of small events [e.g., *Bouchon et al.*, 2013; *Wu et al.*, 2014] reflect detection limits in different environments or may be related to natural variability. As a final example, analyses of earthquake-triggering processes can benefit from improved understanding of limits on detection and resolution of source properties. It is clear that denser networks closer to the target sources have higher detection capabilities, but the limits to detection in various circumstances are not well established because of the complex interaction between source characteristics, propagation effects, and the acquisition system. Similarly, the limits on data requirements for reliable analysis of source properties of small earthquakes recorded with finite bandwidths are not fully appreciated. Some
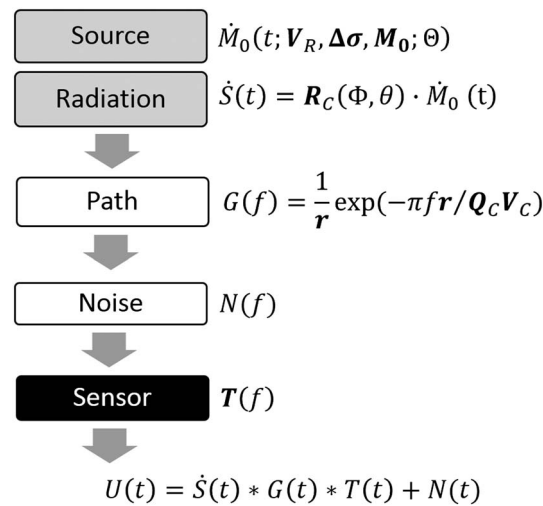
Figure 1. The waveform modeling scheme used in this study together with parameters considered at each simulation step. The key parameters are typed with a bold face. The source is described by seismic moment M_0, (potency P_0) static stress drop $\Delta\sigma$ (strain drop $\Delta\epsilon$) and rupture velocity V_R. The moment rate function $\dot{M}_0(t)$ of P and S waves vary with the angle from the fault normal Θ and the amplitudes are further modified by the radiation pattern $R_C(\Phi, \theta)$. Path effects are described by the source-receiver distance r and intrinsic attenuation Q_C. Seismic noise $N(t)$ is added to synthetic seismograms and recorded waveforms are affected by the transfer function of the sensor $T(f)$.

studies attempted to clarify the limits to detection of seismic events using observed seismic data and simple-yet-practical approach of aggregating the influence of propagation and other effects in "correction factor(s)" [e.g., *Gomberg*, 1991; *Kværna et al.*, 2002]. This data-driven empirical approach is highly valuable but also case specific (e.g., the results depend on properties of the study area, focal coverage, acquisition system, etc.). In the present work we use forward waveform modeling for a large set of parameters to address general basic aspects affecting event detection and ability to analyze earthquake source properties in various situations. The study is based on synthetic calculations of seismic radiation from circular kinematic sources, with consideration of the ambient seismic noise and properties of several common recording systems.

We begin by considering the amplitude and frequency content of waveforms generated by sources that have different properties (size, rupture velocity, stress drop, and shear versus tensile type), examined at observation points in a purely elastic solid. We then analyze modifications to the amplitude and frequency content of the waveforms associated with geometrical spreading and intrinsic attenuation between the seismic source and receiver, as well as instrumental effects and the ambient noise. Properties of P waves are illustrated in the main text and the corresponding properties of S waves are given in the supporting information. We set the detection threshold at a level where the signal-to-noise (S/N) ratio equals 1 (0 dB). This is a natural limit value, although standard network detection often involves S/N ratio > 5 while using matched-filter processing (templates) techniques allows detections at S/N ratio < 0.1 [*Gibbons and Ringdal*, 2006; *Shelly et al.*, 2007]. Plots of S/N ratios of P and S waves in relation to various variables quantify the detectability of events in different situations. The results demonstrate the key influence of magnitude, attenuation, and source-receiver distance on earthquake detection. The results also indicate that the static stress drop and acquisition system properties have significant impact on the detectability of events. The S-to-P wave amplitude ratios are shown to decrease with decreasing magnitudes and to be correlated with the attenuation coefficients of both phases. Together with amplitude and S/N ratio investigations, the expected frequency content of the waves is analyzed and discussed in the context of reliable assessment of source parameters. The presented results provide useful information for design of seismic monitoring networks and for studies concerned with earthquake source physics and scaling relations.

2. Methods

Recorded seismograms can be interpreted as convolutions of source, path, and sensor effects superposed with the ongoing ambient seismic noise. To clarify the limits on detection and seismic source analysis of earthquakes, we model synthetic seismograms using the scheme summarized in Figure 1, add to the generated seismograms random motion based on a defined noise model, and calculate the S/N ratio of P and S waves. In the following subsections we examine how different sets of source, path, sensor, and noise characteristics affect the amplitude and frequency content of seismic waveforms. Synthetic results produced for various values of the parameters listed in Figure 1 are used to assess the likelihood of detecting small events

in different circumstances, as well as to provide bounds on the ability to estimate source properties of the detected events.

2.1. Source Effects
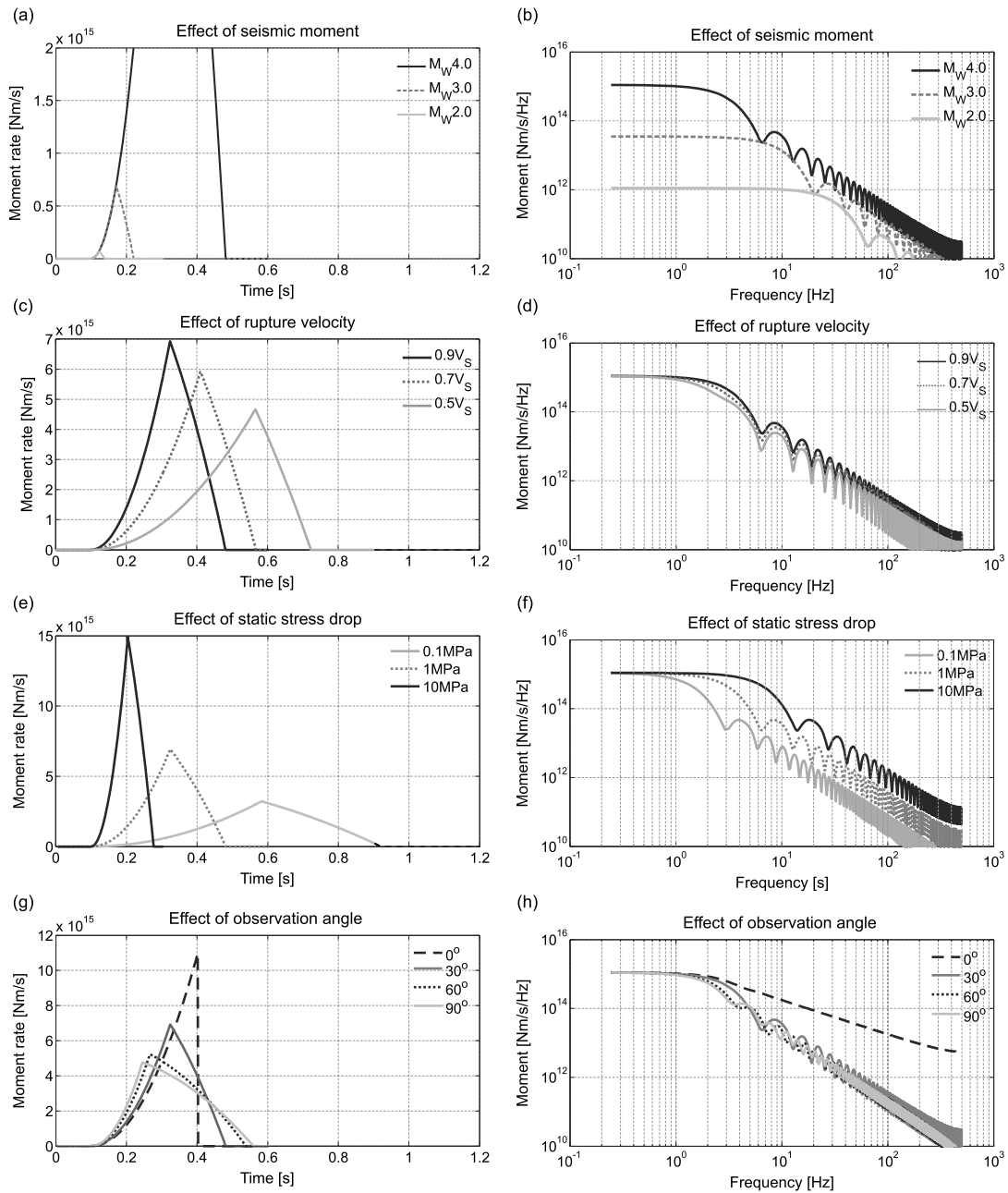
2.1.1. Source Time Function

We simulate source time functions (STFs) using the Sato-Hirasawa (SH) kinematic circular source model [*Sato and Hirasawa*, 1973; *Sato*, 1978], where rupture initiates at a point and spreads radially with a constant rupture velocity V_R. The rupture stops abruptly at some radius L resulting in a static strain drop $\Delta\epsilon$. The circular geometry of the SH model is convenient for describing small earthquakes that are the primary target of this study. The SH seismic source is completely specified by three parameters: the seismic moment M_0, static stress drop $\Delta\sigma$, and rupture velocity V_R. An equivalent parameterization independent of the shear modulus G at the source is the seismic potency P_0 (M_0/G), strain drop $\Delta\epsilon$ ($\Delta\sigma/G$), and V_R. For any assumed seismic moment, static stress drop and rigidity in the source region (or just strain drop), the source radius L used for modeling the STFs can be calculated from the formula of *Eshelby* [1957], $\Delta\sigma = (7/16)M_0L^{-3}$. The source radius is related to the corner frequency through $L = c_c V_C/(2\pi f_C)$ where V_C, f_C, and c_C are, respectively, wave velocity, corner frequency, and model-dependent constant for either P or S waves. We note that the static stress drop values discussed in this study apply strictly to the SH model. Different models lead to different inferred stress drops from the same corner frequency and seismic moment, since they have different constants in the formula connecting the moment and corner frequency to the stress drop. For example, a static stress drop of 1 MPa in the adopted SH model corresponds to 0.62 MPa assuming the model of *Brune* [1970, 1971] and to 3.4 MPa assuming the source model of *Madariaga* [1976]. See *Kaneko and Shearer* [2015] for additional examples associated with other models.

Figure 2 presents the STF or moment rate (Figure 2, left), which is proportional to the far-field amplitude of ground displacement seismograms, and the corresponding source spectra (Figure 2, right) for events with different seismic moments, rupture velocities, and static stress drops. The STFs are shown for receivers located at 30° from the normal to the fault plane and the calculations assume a purely elastic solid (attenuation effects will be examined later). Figures 2a and 2b show the amplitude and frequency content of waveforms for different moment magnitudes. The area below each STF is equal to the seismic moment and corresponds to the amplitudes of the displacement spectrum at low frequencies or the spectral level $\Omega(0)$. As expected, larger magnitudes result in larger amplitudes of the STF, higher $\Omega(0)$ levels and lower corner frequencies. Effects of rupture velocity on the source properties are illustrated in Figures 2c and 2d. With increasing V_R, the STF becomes narrower with higher amplitudes but maintains the same area (reflecting the assumed seismic moment). Similarly, the spectral levels measured at low frequencies in Figure 2d are identical, but increasing rupture velocity leads to somewhat higher frequency content. However, for changes of rupture velocities in the range $0.5 - 0.9$ V_S, the effect on spectral shape is not major. Figures 2e and 2f display effects of variable static stress drops for a fixed moment on the STF and frequency content. Increasing stress drops lead to narrower and higher STFs along with higher corner frequencies. These effects are similar to but more pronounced than what is produced by increasing rupture velocity. This is related to the fact that the variability of stress drop values is much larger than that of rupture velocity (factor of 2 for the rupture velocity versus order of 2 for the stress drop).

2.1.2. Observation Point Directionality

Since the rupture front in the SH model propagates radially with constant velocity, the source has no directivity effects (no asymmetric rupture propagation) and the shape of the STF remains the same for locations with different azimuths in the fault plane. However, the STF shape depends on the observation angle given by the angle Θ between the normal to the fault plane and the receiver. We distinguish this effect from rupture directivity and refer to it as observation point directionality. In the coordinate system used, $\Theta = 0°$ corresponds to observation direction normal to the fault and $\Theta = 90°$ corresponds to observation point located in the fault plane.

Figures 2g and 2h present the influence of observation angle Θ on the amplitude and frequency content of the STF. Similarly to previous considerations, the area below the STF does not change, but higher observation angles produce wider STF with lower amplitudes. Noteworthy, for observation angles located close to the fault normal, the SH model predicts significant deviation from ω^2 source model with ground displacement spectral fall off exponent equal to 1 (cf. Figure 2h). However, in typical scenarios most recorded data involve
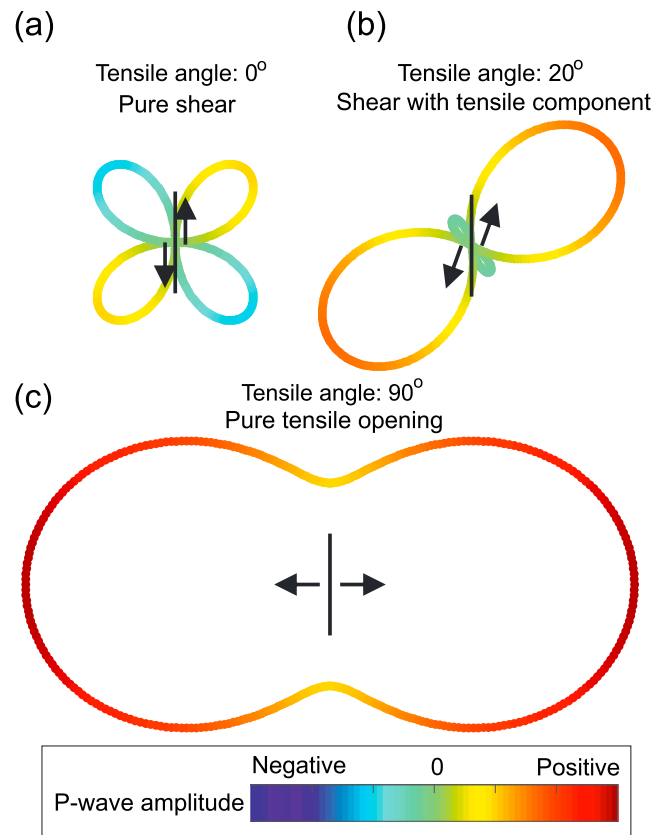
Figure 2. Effects of (a, b) magnitude, (c, d) rupture velocity, (e, f) static stress drop, and (g, h) observation angle on the shape of STF (left) and its spectral properties (right). In each panel source time functions and spectra are plotted for variations of a single parameter (indicated in the top right corner of each panel) and other parameters corresponds to the generic source ($M_W = 4.0$, $V_R = 0.9$ V_S, and $\Delta\sigma = 1$ MPa, observed at $\Theta = 30°$ off the fault normal). The spectra in Figure 2h follow the ω^{-2} source model except for (statistically uncommon) observation angles close to the normal where the spectra falls as ω^{-1}.

observation angles $\Theta > 30°$ and only about 30% of the data are associated with $\Theta < 30°$ [*Sato and Hirasawa,* 1973]. This is because in typical monitoring situations only a limited number of stations are located in the narrow zone above the earthquakes.

2.1.3. Radiation Pattern

The radiation pattern modifies the amplitudes of observed seismograms. It is typically described by a correction factor that depends on the faulting geometry and observation point described by azimuth to the station and takeoff angle (note that the takeoff angle follows the standard seismological convention with values between 0° and 180° for downgoing and upgoing rays, respectively, and is different from the directionality

(a)

Tensile angle: 0°
Pure shear

(b)

Tensile angle: 20°
Shear with tensile component

(c)

Tensile angle: 90°
Pure tensile opening

Figure 3. Map view of the radiation pattern of P phase (strike/dip/rake = 0°/90°/0°) for three values of the tensile angle α: (a) Pure shear source ($\alpha = 0°$), (b) shear source with a tensile opening component ($\alpha = 20°$), and (c) pure tensile opening failure ($\alpha = 90°$). The colored lobes and their distance from the fault (black line) reflect the expected amplitude of P phase observed at different azimuths. The relative motions of two faces of the fault plane are shown with black arrows. The assumed Poisson's ratio is $v = 0.25$ [see *Vavryčuk*, 2001; *Kwiatek and Ben-Zion*, 2013 for details].

parameter Θ described in the previous section). For a pure shear source, the radiation patterns for P and S waves may be averaged when the focal mechanism is not known [*Boore and Boatwright*, 1984]. In this study we use extended radiation pattern formula for a more general shear/tensile source model [*Vavryčuk*, 2001; *Ou*, 2008; *Kwiatek and Ben-Zion*, 2013]. In this model, the source is described by the strike, dip, and rake on the fault plane, along with a tensile angle α between the slip vector and its projection on the fault surface. The tensile angle allows simulating nondouble-couple faulting mechanisms that are frequently reported for small earthquakes. The value $\alpha = 90°$ corresponds to pure tensile opening, $\alpha = -90°$ corresponds to pure tensile closing, and $\alpha = 0°$ corresponds to pure shear along the fault plane. Three example radiation patterns of P waves are given in Figure 3.

Figure 4 illustrates STFs for several source tensile angles and various locations of the observation point. The maximum amplitude of the source pulse increases with increasing tensile angle regardless of the observation point. We note that for each tensile angle the maximum amplitude occurs at a different observation angle.

2.1.4. Average Effect of Source, Directionality, and Radiation Pattern

It is evident that the maximum amplitude of the STF (and thus the earthquake detection) depends primarily on the earthquake magnitude. However, as seen in the forgoing results, the static stress drop, rupture velocity, tensile angle, and radiation pattern modify both the amplitude and spectral characteristics of the STF. To reduce the number of variables in the subsequent parameter-space study, we now investigate the effects of static stress drop, rupture velocity, and faulting type on the maximum pulse amplitude averaged over all observation points and all possible focal mechanisms.

For given rupture velocity and static stress drop ($\Delta\sigma = 0.1, 1, 10$ MPa) we generate a set of 10,000 STFs $\{STF^i(t)\}_{i=1\ldots10000}$ observed at randomly sampled observation angles Θ_i and azimuths Φ_i using a sampling procedure based on the Monte Carlo approach [*Sato and Hirasawa*, 1973; *Boore and Boatwright*, 1984]. The generated STFs are corrected for radiation pattern through multiplication with a radiation pattern correction coefficient $R_P(\Phi_i, \theta_i)$. Here we consider two end-member focal mechanisms—pure shear faulting ($\alpha = 0°$) and pure tensile opening ($\alpha = 90°$)—and randomly sample the remaining fault plane parameters. For each calculated case we extract the maximum amplitude of the STF derivative, $v^i_{max} = \max(\dot{STF}^i(t))$, which is proportional to the maximum far-field ground velocity. The set of maximum velocity amplitudes, parameterized by the rupture velocity, static stress drop, and tensile angle is used to calculate the root-mean-square (RMS) of the maximum amplitude
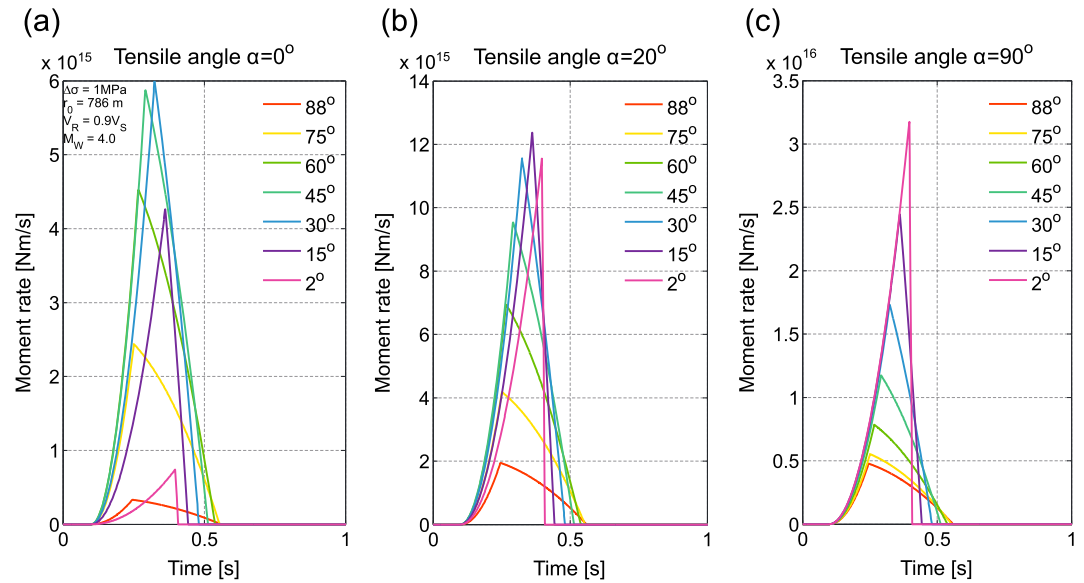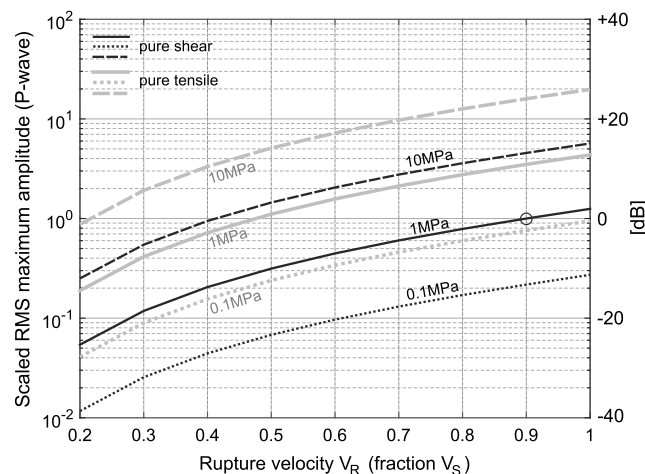
Figure 4. Comparison of STFs including radiation pattern correction at various observation points ($\Theta = 2°$, 15°, 30°, 45°, 60°, 75°, 88°) for different tensile angles: (a) Pure shear source ($\alpha = 0°$), (b) shear source with tensile component ($\alpha = 20°$), and (c) pure tensile failure ($\alpha = 90°$).
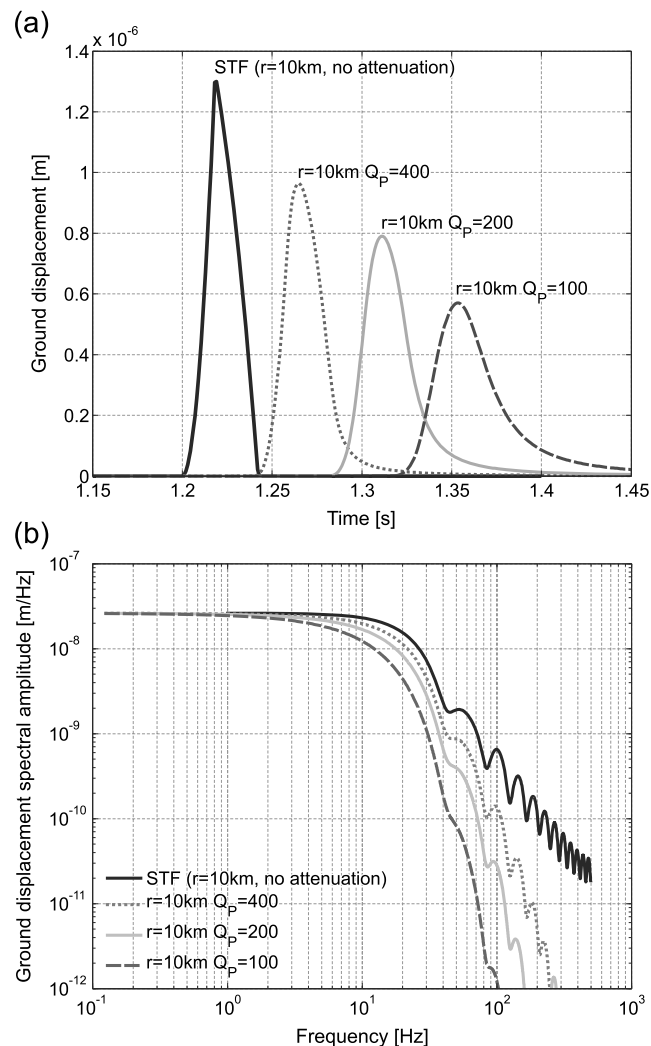
$v_{max}^{rms} = \mathrm{rms}\left(\left\{v_{max}^i\right\}_{i=1\ldots10000}\right)$. This effectively gives the maximum RMS amplitude averaged over all observation points and focal mechanisms.

Figure 5 presents the dependency between the rupture velocity and RMS of maximum P wave amplitude. Each curve is parameterized by different static stress drops and end-member faulting types. The RMS maximum amplitudes are scaled to that of a *standard source* defined as a seismic shear source with $\Delta\sigma = 1$ MPa and $V_R = 0.9$ V_S (black circle in Figure 5), essentially making the results magnitude independent. The results show average variations of expected maximum ground velocity with respect to that of the standard source.

For example, for a pure shear event with rupture velocity $V_R = 0.6$ V_S and stress drop $\Delta\sigma = 10$ MPa, we may expect on average nearly 2 times larger maximum ground velocity regardless of particular focal mechanisms and observation points. Similarly, for pure shear event with rupture velocity $V_R = 0.5$ V_S and static stress drop of $\Delta\sigma = 0.1$ MPa we expect on the average 17 times lower maximum ground velocity compared to the standard source. These results indicate that assuming a pure shear source and reasonable ranges of static stress drop (0.1–10 MPa) and rupture velocity (0.5–0.9 V_R), the maximum ground velocity may vary between −23 dB and +14 dB regardless of focal mechanism and observation point. For a pure tensile source (gray curves in Figure 5), the P wave amplitudes are persistently

Figure 5. Dependence between rupture velocity and maximum STF derivative amplitude (proportional to far-field ground velocity) RMS averaged over all focal mechanisms and observation angles. The values are scaled to the maximum RMS amplitude observed for a standard source with $V_R = 0.9$ V_S and $\Delta\sigma = 1$ MPa (open black circle). The curves are parameterized by different static stress drop (0.1–10 MPa) and failure model (pure shear, pure tensile faulting). See text for details.

(a)

(b)

Figure 6. (a) Time and (b) frequency domain illustrations of attenuation effects. The STF at the 10 km distance and not affected by attenuation is shown as thick black line. The remaining curves display low-pass filtering attenuation effects at 10 km distance assuming $Q_P = 400$, 200, and 100.

enhanced by approximately +11 dB regardless of the stress drop and rupture velocity. For S waves, the radiation is very similar regardless of the faulting type. To conclude this part, the magnitude is the dominant factor affecting the maximum amplitude of far-field signals. The magnitude-independent variations due to reasonable expected changes in the static stress drop and rupture velocity for all focal mechanisms are in the range −23 dB to +14 dB.

2.2. Path Effects
2.2.1. Geometric Spreading
Since we are concerned here with body waves in the far field, we assume that the amplitude of the source waveform is diminished by a factor of 1/r, where r it the source-receiver distance.
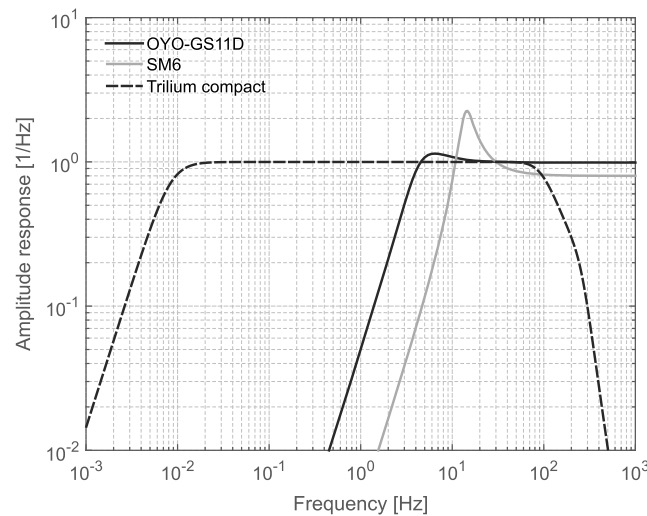
2.2.2. Intrinsic Attenuation
The intrinsic attenuation accounting for deviations from pure elasticity can affect significantly the amplitude and frequency content of recorded waveforms. We assume that the intrinsic attenuation depends on the wave type (P or S) but is frequency independent. In the frequency domain, the attenuation operator takes the form

$$Q_C(f) = \exp\left(-\frac{\pi f r}{V_C Q_C}\right), \quad (1)$$

where V_C and Q_C are the velocity and dimensionless quality factor

of either P or S wave, respectively. To implement the attenuation effects, we use the time-domain representation of the attenuation operator [*Futterman*, 1962]. The effects of attenuation are illustrated in Figure 6 in the time and frequency domains using an example STF and several Q_P values for sensors located 10 km away from the hypocenter. It is evident that the attenuation reduces significantly the amplitude and high-frequency content of waveforms away from the source.

2.3. Instrumental Effects
Recorded ground motions are convolved with the instrument response (transfer function) and are sampled at a given sampling interval. Both of these effects act essentially as a band-pass filter, reducing the amplitude of frequencies below the natural frequency of the sensor and above a limiting frequency that is somewhat below the Nyquist frequency of the sampling rate. The resulting reductions in amplitude and frequency content of recorded waveforms diminish further the event detectability. We investigate the instrumental effect on earthquake recordings for the following three different sensors: SM6 short-period sensor with natural frequency $f_n = 15$ Hz, OYO Geospace short-period geophone GS11D with $f_n = 4.5$ Hz, and Trilium Compact broadband sensor with $f_n = 0.008$ Hz. The amplitude transfer functions of these sensors are shown in Figure 7.

Figure 7. Transfer functions of sensors used to simulate the instrumental effects on recorded ground motions.

2.4. Seismic Noise

Peterson [1993] compiled two global background noise models describing the expected low (NLNM) and high (NHNM) noise levels in the frequency range 10^{-5} Hz and 10 Hz. Since the focus of this work is on small events, the Peterson's noise model should be extended to much higher frequencies to be useful for the detection and source analyses. Unfortunately, to our knowledge there is no thorough compilation of observed noise at higher frequencies. We therefore augment the Peterson's noise model with data from the following instruments and locations (Table 1): two short-period borehole sensors located about 500 m and 1100 m below the surface in the Berlín Geothermal Field, El Salvador [*Kwiatek et al.*, 2014], high-frequency geophone at a depth of 4 km in the Gross Schoenebeck, Germany [*Moeck et al.*, 2009; *Kwiatek et al.*, 2010], short-period and broadband surface sensors at The Geysers geothermal field [*Kwiatek et al.*, 2015]; short-period sensors installed in Rudna Copper Mine, Poland, and data recorded by a spatially dense array of 10 Hz geophones on the San Jacinto fault zone [*Ben-Zion et al.*, 2015].

Figure 8 presents noise recorded at the sites listed in Table 1 up to 1000 Hz together with the high and low noise models of Peterson and the geometrical mean of the noise data. Two features of the noise above 10 Hz are notable. First, the noise levels differ with generally (but not always) higher and lower noise levels observed at surface and borehole stations, respectively. The noise level recorded by surface instruments at the San Jacinto fault with heavily damaged rocks [*Allam et al.*, 2014; *Zigone et al.*, 2015] is lower than the levels observed with some borehole and underground sensors, probably because of the larger attenuation around the San Jacinto Fault. In addition, the noise level appears to decrease with frequency at some sites, while at others it remains similar up to a few hundreds of hertz. In the subsequent analysis we use the geometrical mean from the available noise data (marked in Figure 8 as a thick black dotted line). Amplitude power spectral density given by this line is combined with random-phase information to generate noise traces in the time domain by means of inverse Fourier transform. These noise traces are used to perturb the synthetic seismograms in the subsequent results.

2.5. Event Detection

The source, path, instrument, and noise effects are combined to generate synthetic seismograms and measure the signal-to-noise ratio (cf. Figure 1). The STF is parameterized by the seismic moment M_0 (potency P_0), stress drop $\Delta\sigma$ (strain drop $\Delta\epsilon$) over the fault and rupture velocity V_R. The amplitude of the STF is modified by the P or S wave radiation pattern $R_C(\Phi, \theta)$ averaged over all fault plane parameters and observation points. We

Table 1. A Summary of Sensor Characteristics Used to Investigate Noise Levels

Site	Sensor	Location	Sampling Rate (Hz)
Gross Schoenebeck, Germany	HS-11 15 Hz	Borehole (4 km)	1000
The Geysers, California	GS11D 4.5 Hz	Surface	500
	Trilium Compact 0.008 Hz	Surface	200
Rudna Copper Mine, Poland	GS11D 4.5 Hz	Underground (1 km)	500
San Jacinto Fault Zone	ZLand 10 Hz	Surface	500
Berlín Geothermal Field, El Salvador	IMS sensors 1 Hz, 4.5 Hz, 5.5 Hz	Boreholes (0.5–1.1 km)	500–3000
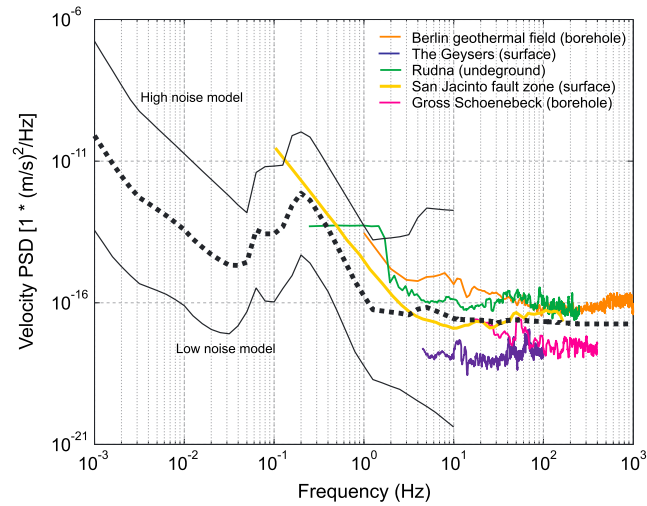
Figure 8. Comparison of noise levels recorded at different sites with borehole or surface sensors. The low and high Peterson noise models are shown with solid black lines. The noise model used in this study combined from low- and high-frequency noise information is denoted by the thick dotted line.

consider two end-member faulting types: pure shear with $\alpha = 0°$ and pure tensile opening with $\alpha = 90°$. For the pure shear source, the amplitude of the STF is modified by average factors $R_P = 0.52$ and $R_S = 0.63$ for the P and S waves, respectively [*Boore and Boatwright*, 1984]. For the pure tensile source, the P wave radiation in enhanced considerably leading to average correction factor $R_P = 1.75$, while the radiation of S waves increases slightly and is associated with $R_S = 0.73$ [*Kwiatek and Ben-Zion*, 2013]. The resulting radiated source pulse is subjected to geometrical spreading and intrinsic attenuation associated with a quality factor Q_C. The pulse shape is affected further by the sensor's transfer function and the sampling rate of the acquisition system. In the final step of producing synthetic data, a noise trace generated from the power spectral density of the average noise model of Figure 8 is added to the pulse wavelet. The medium is assumed isotropic with the following parameters: P wave velocity $V_P = 5000$ m/s, Poisson's ratio $\upsilon = 0.25$, shear modulus $G = 30$ GPa, and $V_S = V_P/\sqrt{3}$. These values are representative for crustal rocks. The values of the attenuation coefficients are specified below.

To simulate waveform preprocessing, the resulting synthetic seismograms are filtered by a fourth-order 1–1000 Hz band pass Butterworth filter to remove low-frequency oscillations and high frequencies. The low-frequency limit of the filter is reasonable if one focuses on detection of earthquakes with $M_W < 4.0$. The high-frequency corner accounts for antialiasing filter of acquisition system operating at relatively high sampling frequencies. After filtering, the noise level is measured on the synthetic ground velocity waveform as the standard deviation of the record preceding the arrival from the source. The amplitude of the earthquake signal is measured as the maximum ground velocity amplitude in the synthetic seismogram. The S/N ratio is calculated from these two parameters as

$$S\big/N[dB] = 20 \log_{10} \frac{\max(V(t))}{\mathrm{rms}(N(t))}, \qquad (2)$$

where $V(t)$ and $N(t)$ are the ground velocity seismogram and noise in the time domain, respectively. For each set of parameters describing the source, path, and sensor effects, the S/N ratio is calculated 100 times using randomly selected noise traces added to the synthetic signal and then averaged. An S/N ratio of 20 dB signifies an amplitude of recorded source arrival that is 10 times higher than the noise level. For an earthquake detection threshold, we require the maximum amplitude of the source arrival to be equal to that measured in the preceding noise level, i.e., an S/N ratio of 0 dB.

In addition to the S/N ratio, the *observed* corner frequency of either the P or S signal is calculated using the following integrals [*Andrews*, 1986; *Snoke*, 1987]:
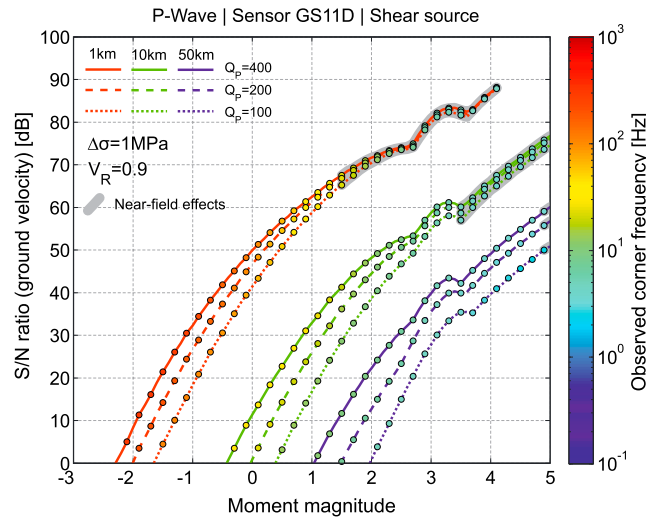
Figure 9. Dependence between moment magnitude and S/N ratio assuming standard shear source ($V_R = 0.9 V_S$ and $\Delta\sigma = 1$ MPa) including sensor characteristics of GS11D sensor (cf. Figure 7). Solid, dashed and dotted lines correspond to low, medium, and high attenuation with $Q_P = 400$, 200, 100, whereas red, green, and blue colors correspond to increasing source-receiver distances $r = 1$ km, 10 km, 50 km, respectively. The filled circles mark *observed* corner frequency. The bulge in all curves around M_W 3.0 reflects the increased sensitivity of GS11D sensor around 1 Hz natural frequency (cf. Figure 7). The thick gray lines emphasize data points where S/N ratio may be affected by near-field effects (see text for details).

$$J = 2\int_0^\infty [V(t)]^2 dt,$$
$$K = 2\int_0^\infty [U(t)]^2 dt, \qquad (3)$$
$$f_C^{obs} = \frac{1}{2\pi}\sqrt{\frac{J}{K}},$$

where $U(t)$ is the ground displacement seismogram and the J and K integrals are corrected for the limited frequency band of the considered spectra [e.g., *Di Bona and Rovelli*, 1988]. We refer to the calculated corner frequency as observed (not *source*), since it reflects the dominant frequency of the observed signal and it is not a true source property. To calculate the source corner frequency, appropriate corrections for path and sensor effects have to be applied first.

3. Results

3.1. Earthquake Detection

Figure 9 presents S/N ratios of the observed *P* wave pulse in velocity seismograms for synthetic earthquakes with different moment

magnitudes, assuming a *standard* seismic source with rupture velocity $V_R = 0.9 \, V_S$ and stress drop $\Delta\sigma = 1$ MPa. The curves are parameterized by different source-receiver distances ($r = 1$, 10, and 50 km) and different quality factors of *P* waves ($Q_P = 100$, 200, 400). To simulate the acquisition system we use the transfer function of GS11D sensor (cf. Figure 7). The applied band-pass filter affects slightly the amplitudes for the largest and the smallest earthquakes. Corresponding results for *S* waves, other sensors types, rupture velocities, and stress drops are provided in the supporting information. The presented results focus on the far field where $r \gg L$ and $r \gg \lambda$ with L and λ being source dimension and wavelength of interest [e.g., *Ben-Zion*, 2003]. Although most seismometers are in the far field, data recorded by local networks include near-field terms that can enhance the ability of extracting information from the data [e.g., *McGarr*, 1991; *McGarr and Fletcher*, 2002]. Since near-field terms are not accounted for in our results, we do not consider locations with $r < L$ and highlight in Figure 9 and following figures, data points that may be affected by near-field terms with thick gray lines.

As expected, the source-receiver distance and attenuation are major effects governing the recorded S/N ratios, with attenuation having an increasing effect at larger source-receiver distances. At 50 km distance, events with moment magnitude $M_W < 1.5$ are not detectable for $Q_P < 200$. For comparison, at 1 km distance earthquakes with $M_W = -2.0$ are hardly detectable for $Q_P \approx 200$, while for $Q_P = 100$ only events with $M_W > -1.6$ have *P* pulse signal above the noise level. The visible bulge in all curves around $M_W 3.0$ is related to increased sensitivity of GS11D sensor at its natural frequency.

Although Figure 9 corresponds to specific source properties, it may be combined with Figure 5 to provide approximate estimates of S/N ratios for other source characteristics. In general, earthquakes with higher stress drops and rupture velocities excite narrower STFs with larger amplitudes, leading generally to higher S/N ratio, although the precise values depend on source-receiver distance, attenuation, and sensor effects. These parameters affect the frequency content as well. Earthquakes with larger tensile component excite larger *P* waves (in this case the frequency content is not affected) so pure tensile events have approximately 4 times larger *P* wave amplitudes than corresponding shear events (cf. Figure 5). This increases the S/N ratio of *P* waves by approximately +12 dB, and in consequence leads to tensile events being more easily
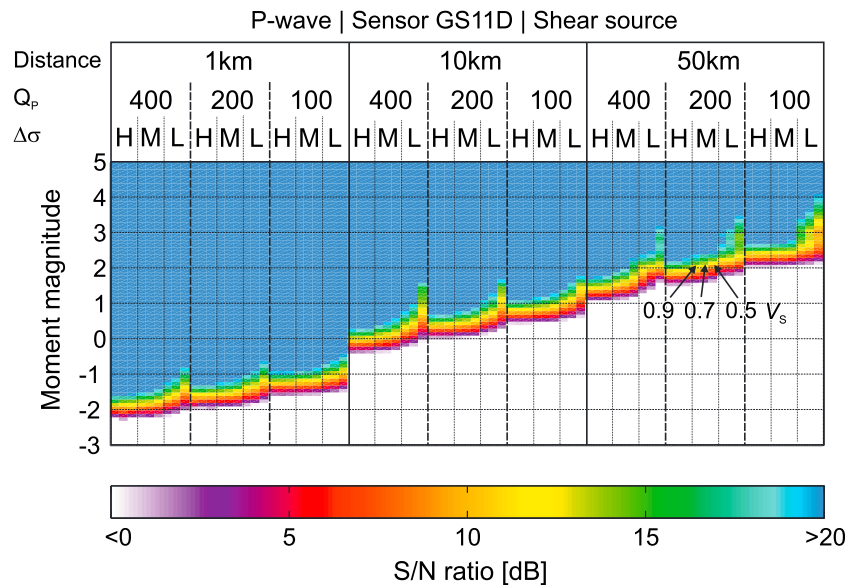
Figure 10. Event detection capability of a shear source using *P* waves and GS11D sensor. The color scale corresponds to S/N ratio of the ground velocity first *P* wave pulse in (dB) with white color (S/N ≤ 0 dB) marking the assumed detection level. Each column corresponds to different seismic source and path properties including source-receiver distance, attenuation, stress drop, and rupture velocity. The stress drop is labeled H, M, and L for 10 MPa, 1 MPa, and 0.1 MPa static stress drops, respectively. The rupture velocity is ordered in each subcolumn of H, M, and L, from 0.9, 0.7, and 0.5 V_S. Similar figures for other sensors and *S* phases are presented in the supporting information.

detectable. However, earthquakes with pure tensile opening are unlikely and the expected enhancement of S/N ratio due to realistic tensile components is likely considerably below 12 dB. Large tensile components are only observed in underground explosions or small earthquakes associated with, e.g., mining or fluid injection activity. However, even in such cases α is generally expected to be below 40°, producing approximately 80% non-double-couple component of the seismic moment tensor [*Vavryčuk*, 2001].

Figure 10 summarizes detection results for pure shear events with various static stress drops, rupture velocities, propagation distances, and *P* wave attenuation coefficients assuming GS11D sensor. The S/N ratios (color scale) reflect the detectability of events with different sets of source and path characteristics. At 1 km hypocentral distance, with the assumed acquisition system and preprocessing, $M_W > -1.6$ events are detectable in far-field environment with $Q_P > 100$ using *P* waves. For 10 km source-receiver distance, the detection level increases on average to M_W 0.5 events. Within these relatively close source-receiver distances the effects of attenuation, stress drop, and rupture velocity are not very significant, but they become important at larger distances. For 50 km hypocentral distance, the detection level of events characterized by low static stress drop and rupture velocity in high-attenuation solid can differ by more than a full magnitude unit from that of events with high stress drops and high rupture velocity in low-attenuation medium. For example, a M_W2.0 earthquake with 0.1 MPa static stress drop and low rupture velocity ($V_R = 0.5$ V_S) in a solid with $Q_P = 100$ is barely detectable at 50 km using *P* waves and GS11D sensor, while the same magnitude event with $\Delta\sigma = 10$ MPa and high rupture velocity is easily detectable in a solid with $Q_P = 400$.
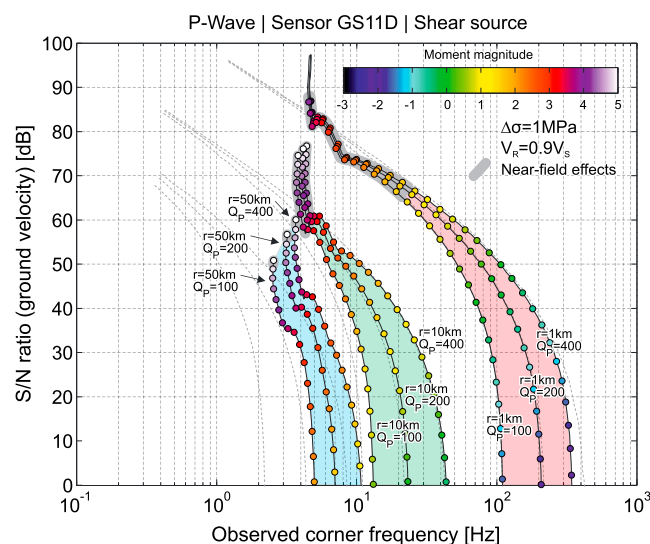
3.2. Frequency Content and Reliable Assessment of Source Parameters

Figure 11 presents relations between the observed *P* wave corner frequency and the S/N ratio assuming a standard shear source with rupture velocity $V_R = 0.9$ V_S and stress drop $\Delta\sigma = 1$ MPa and neglecting sensor effects. Each curve is parameterized by different source-receiver distances $r = 1, 10,$ and 50 km and *P* wave quality factors $Q_P = 100, 200, 400$. The observed corner frequency is calculated following equation (3). The results illustrate the expected dominant frequency of the signal that may be observed in isotropic solid for the ranges of assumed parameters. This may be used to assess the most desirable sensor characteristics to efficiently capture and analyze earthquakes in a certain magnitude (or equivalent frequency) range. Recording data in a frequency band from near zero to 3 times the corner frequency is essential for a reliable
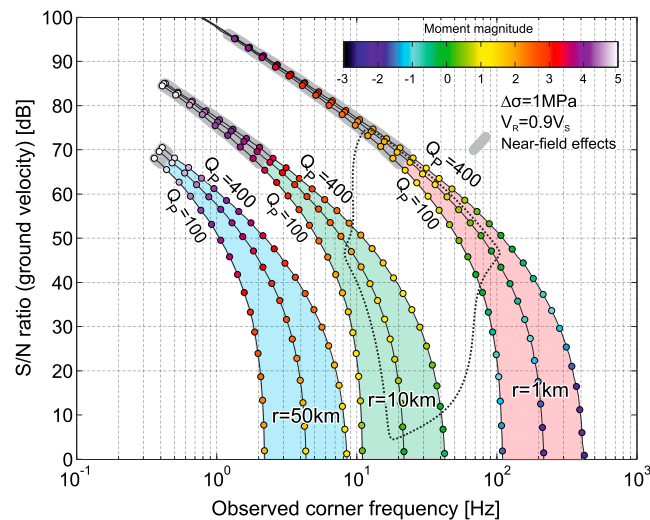
Figure 11. Dependence between observed corner frequency calculated from P waves and S/N ratio for a standard shear source ($V_R = 0.9V_S$ and $\Delta\sigma = 1$ MPa). Each curve is parameterized by different values of source-receiver distance and quality factor. Instrumental effects are not considered so the corner frequency depends on source effects, geometrical spreading, and attenuation. The moment magnitude is given by the color scale. The thick gray lines emphasize data points where S/N ratio may be affected by near-field effects (see text for details).

assessment of source parameters [*Abercrombie*, 2015]. Similar plots for other source characteristics (stress drop, rupture velocity) are presented in the supporting information. As an example, consider a region characterized by $Q_P = 200$ and earthquakes with static stress drops of 1 MPa. If the target magnitude range is 0.0–2.0 and the monitoring distance range is 1–10 km (black-dotted polygon in Figure 11), the expected observed frequency range is 10–100 Hz and sensors should record effectively at least up to 300 Hz. This suggests using in this case short-period sensors with sampling rates exceeding 600 Hz.

Figure 12 displays similar results to those of Figure 11, with the added incorporation of the transfer function of GS11D sensor (similar plots for other source characteristics and sensors are presented in the supporting information). The results illustrate how the high-pass filtering properties of the GS11D sensor affect the low-frequency content of the observed waveforms. This leads to a significant bias in the observed corner frequencies of events larger than about $M_W = 3.0$. The instrumental event cutoff is larger for the SM6 sensor which has higher natural frequency (see supporting information).

Comparing Figure 12 (and related plots in the supporting information for other sensors) with Figure 11 provides first-order information at which frequencies/magnitudes we may expect a bias in quantities derived from seismograms associated with different source, path, and acquisition system characteristics.

In typical analyses of source parameters, the calculated ground velocity or displacement spectra are corrected for the sensor characteristics. This leads to enhancement of the recorded signals at frequencies below the natural frequency of the sensor, which could have allowed in the absence of noise for correct estimates of corner frequencies, seismic moment/potency and other source characteristics (cf. Figures 11 and 12). However, certain frequencies are masked by the noise so not

Figure 12. Dependence between observed corner frequency calculated from P waves and S/N ratio for a standard shear source ($V_R = 0.9V_S$ and $\Delta\sigma = 1$MPa) in calculations assuming instrument effects of the GS11D sensor. Each curve is parameterized by different values of source-receiver distance and quality factor. The moment magnitude is color coded. The light gray dotted lines denote S/N ratios without accounting for sensor characteristics (cf. Figure 7). The thick gray lines emphasize data points where S/N ratio may be affected by near-field effects (see text for details).
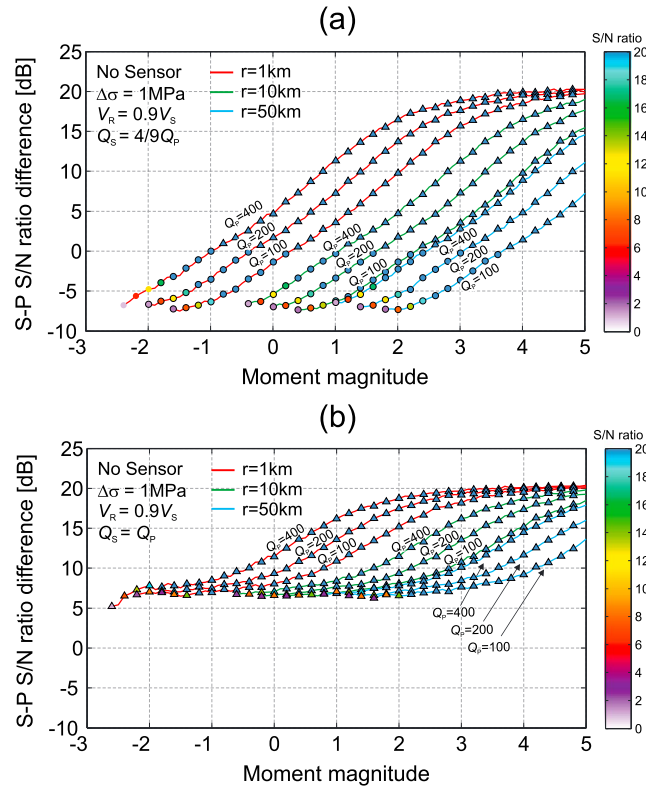
(a)

(b)

Figure 13. Differences between S/N ratios of *S* and *P* waves for standard seismic sources with different moment magnitude assuming (a) $Q_S = 4/9\,Q_P$ and b) $Q_S = Q_P$. Sensor effects are not incorporated. Triangles and circles denote, respectively, whether *S* or *P* wave amplitude is larger with color reflecting the S/N ratio of either the *S* or *P* amplitude.

the entire signal spectrum can be recovered. For example, in a medium with $Q_P = 100$, detection of $M_W 3.0$ earthquake ($\Delta\sigma = 1$ MPa, $V_R = 0.9\ V_S$) using *P* phase at 50 km distance by a short-period SM6 sensor is hardly possible (supporting information) due to the insufficient S/N ratio combined with inappropriate sensor characteristics.

3.3. Earthquake Detection Using *S* Phases

As reviewed by *Kwiatek and Ben-Zion* [2013], the radiated seismic energy from shear sources associated with *S* waves (E_S) is generally significantly higher than the energy (E_P) carried by the *P* waves [cf. *Haskell*, 1964; *Sato and Hirasawa*, 1973; *Madariaga*, 1976; *Venkataraman and Kanamori*, 2004]. For example, in the case of the SH circular shear source model, $E_S/E_P = 24.4$ for $V_R = 0.9\ V_S$ and $E_S/E_P = 17.8$ for $V_R < 0.7\ V_S$. However, for circular tensile SH source model, the $E_S/E_P = 1.1$, regardless of the rupture velocity [*Sato*, 1978] and rock fracturing generating damage-related radiation [*Ben-Zion and Ampuero*, 2009] may lead to $E_P > E_S$. The radiation patterns of *P* and *S* waves are different leading to altered average radiation pattern correction coefficients (see overview by *Kwiatek and Ben Zion* [2013]). The amplitude differences between the *P* and *S* waves are accompanied by slight changes in the frequency content of recorded seismograms. The corner frequency of *S* waves in the SH and other standard models is lower than that of *P* waves with f_P/f_S ratios ranging 1.29–1.39 for rupture velocities in the range $V_R = 0.5 - 0.9\ V_S$ [*Sato and Hirasawa*, 1973] (see also overview in *Kwiatek and Ben-Zion* [2013]). Faulting associated with rock damage and/or tensile source components may produce f_P/f_S ratios higher than 2 [*Yang and Ben-Zion*, 2016].

Another important factor affecting the amplitude and frequency content of recorded seismograms is attenuation. It is typically assumed that *S* waves are more attenuated than *P* waves. If there is no dissipation in pure compression, the theoretical ratio between quality factors of *P* and *S* phases is [*Knopoff*, 1964; *Burdick*, 1978]

$$\frac{Q_P}{Q_S} = \frac{3}{4}\frac{V_P^2}{V_S^2}. \tag{4}$$

For a Poisson solid with $\lambda = \mu$, equation (4) predicts Q_P that is 2.25 higher than that of Q_S [*Burdick*, 1978]. However, observations frequently provide considerably lower Q_P/Q_S ratios [*Olsen et al.*, 2003; *Hauksson and Shearer*, 2006; *Kwiatek et al.*, 2011, 2015] assumed to reflect effects of pore fluids on the attenuation.
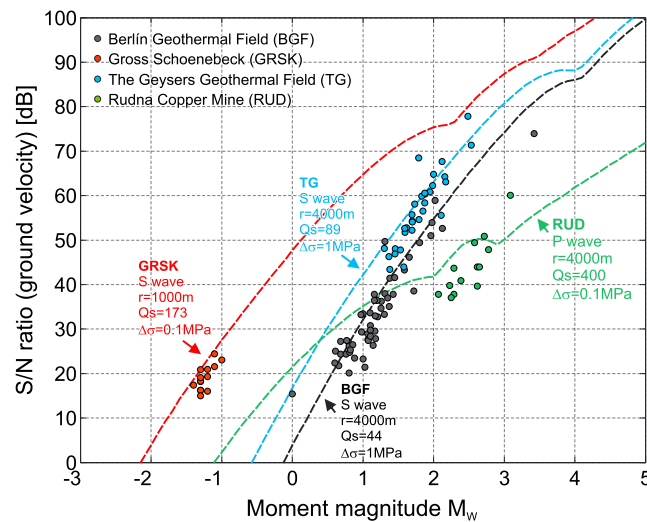
As both amplitude and frequency content of *S* waves are different from those of *P* phases for same source parameters (seismic moment, static stress drop, and rupture velocity), we perform identical modeling for

Figure 14. Comparison of S/N ratios estimated from real ground velocity waveforms (dots) with theoretical predictions of S/N ratio (dashed lines) for four different data sets, plotted as a function of the moment magnitude (cf. Figure 9). The theoretical curves were calculated using available information on source (stress drop), path (attenuation), and sensor parameters that correspond best to the specific site (framed colored texts). The observed S/N ratios were calculated using seismograms of earthquakes located within a certain distance interval from hypocenters to match the synthetic S/N ratio curves (±10% of indicated distance).

S/N ratio determination using S waves and assuming $\lambda = \mu$, $V_S = V_P / \sqrt{3}$. We consider two relations between the quality factors of P and S waves: $Q_S = 4/9\ Q_P$ (equation (4)), and $Q_S = Q_P$.

Figure 13a presents differences of the S/N ratios associated with S and P waves for standard seismic sources ($\Delta\sigma = 1$ MPa and $V_R = 0.9\ V_S$) with different moment magnitudes and no sensor effects (figures for other values of static stress drop and rupture velocity are shown in supporting information). The results assume $Q_S = 4/9\ Q_P$ and are parameterized for different source-receiver distances and attenuation. Figure 13b provides corresponding results assuming $Q_S = Q_P$.

The most interesting feature visible regardless of whether $Q_S = 4/9\ Q_P$ or $Q_S = Q_P$ has been used is the persistent decrease in the difference between the S/N ratios of S and P waves with decreasing moment magnitude (or equivalently reduced S/P amplitude ratio with decreasing moment magnitude). The S/N ratio difference saturates at 20 dB for higher moment magnitudes regardless of the source and path properties. The observed saturation level corresponds to radiated energy ratio $E_S/E_P = 24$, which is expected for the SH shear source [*Sato and Hirasawa*, 1973]. The saturation at 20 dB S/P amplitude ratio is faster for shorter source-receiver distances and lower attenuation (cf. parameterization of different curves in Figure 13). The S/P ratio is also observed to saturate at 20 dB earlier at higher magnitudes for sources with lower rupture velocity and lower stress drop (supporting information). The decrease in S/P amplitude ratio is clearly attributed to the low-pass filtering properties of the attenuation operators of P and S waves with respect to the radiated frequency content from the seismic source. Lower frequency content of the generated waves (larger magnitudes, lower stress drop, and lower rupture velocity), combined with shorter source-receiver distances and lower attenuation, results in less severe dropdown in S/P amplitude ratio from the generic 20 dB value. Interestingly, cases with $Q_S = 4/9\ Q_P$ sometimes lead to theoretical predictions of P amplitudes larger than those of S waves (circles in Figure 13a) even for shear sources, with P but not S amplitudes above the noise level. However, when $Q_S = Q_P$ is used, the S wave amplitudes are never below the P wave amplitudes (Figure 13b) and they saturate at lower magnitudes at approximately 7 dB.

3.4. Comparison of Synthetic and Observed S/N Ratios

To perform a basic validation of the theoretical results, we compare the synthetic predictions of S/N ratios with corresponding results based on observed ground velocity recordings in different geological environments (Figure 14). For that purpose we use high-quality microseismic data from four different sites where source parameters were analyzed previously: (a) Berlín Geothermal Field, El Salvador [*Kwiatek et al.*, 2014], (b) Gross Schoenebeck Geothermal Laboratory, Germany [*Kwiatek et al.*, 2010], (c) The Geysers Geothermal Field, United States [*Kwiatek et al.*, 2015], and (d) Rudna Copper Mine, Poland [*Orlecka-Sikora et al.*, 2009]. Depending on data availability, we pick the ground velocity first pulse amplitudes of either S (data sets a–c) or P (data set d) waves, and calculated the S/N ratio using recorded noise. We select seismograms for which source-to-receiver distances are close to 4000 m for data sets a, c, and d, and 1000 m for data set b. For each earthquake, the amplitudes of first P or S wave pulses observed at the different stations are averaged

and plotted versus the moment magnitude of the event (dots in Figure 14). The synthetic S/N ratio curves in Figure 14 employ data set-specific information on attenuation, static stress drop, and sensor characteristics from *Orlecka-Sikora et al.* [2009] and *Kwiatek et al.* [2010, 2014, 2015]. In all simulations we assume $V_R = 0.9V_S$ due to lack of information on the rupture velocities.

As seen from Figure 14, our synthetic simulations of S/N ratios reproduce statistically the observed S/N ratios over a broad magnitude range. This is especially the case for data sets (a, c) for which the uncertainties could be reduced due to the availability of many high-quality stations. Even the observed S/N ratios extracted from a single downhole sensor installed in Gross Schoenebeck fit well the synthetic predictions, likely because the close source-receiver distances result in clear waveforms. In the case of Rudna Copper Mine we note that the observed S/N ratios are overall lower than the predicted ones. This is likely related to the generally increased noise level in the mine due to exploitation. Also, the network in the Rudna Copper Mine consists of vertical sensors located at the level of exploitation where the seismicity also occurs. This results in high incidence angles of waves to the vertical sensors, which diminish the amplitudes and reduce the observed S/N ratios.

4. Discussion

We investigate theoretical time domain and spectral properties of *P* and *S* seismic signals in relation to source, path, and sensor effects, in an effort to clarify limits to event detection and analyses of earthquake source properties. The study is based on a large parameter-space study involving over 59,000 simulated cases (Table S1 and Figures S1–S69 in the supporting information) covering broad ranges of earthquake magnitudes, static stress drops, rupture velocities, and two end-member faulting styles (pure shear and pure tensile faulting). The synthetic *P* and *S* source waveforms are convolved with Green's functions associated with several sets of attenuation coefficients, combined with expected ambient seismic noise up to 1 kHz (Figure 8), and convolved with transfer functions of three different common sensors. The simulated results provide a platform for identifying with far-field seismic data the predominant factors affecting the quality of seismic signals for analysis of source properties and detection of earthquakes in various circumstances.

The S/N ratios of *P* and *S* waves and spectral characteristics of the signals at various source-receiver distances in various structural models are presented in a number of summary plots (Figures 9–13). The overall characteristics of the predicted S/R ratios reproduce well statistically observed S/R ratios extracted from seismograms recorded in four different test regions (Figure 14). However, not all source-structure-sensor characteristics and their effects on seismic signals could be presented, to keep reasonable level of generality. First of all, to discuss earthquake detection and analysis of source properties we assumed constant upper and lower limits of the recorded frequencies by imposing band-pass filter of 1–1000 Hz. The applied filter was set up to efficiently handle the broad magnitude range discussed in the paper, but it diminishes slightly the S/N ratio of larger earthquakes with $M_W > 4.0$ as well as smaller events with $M_W < -3.0$. Also, the recorded waveforms depend clearly on a predefined sampling rate of the acquisition system, which constrains the upper frequency limit of the recorded frequencies. If the sampling rate is too low, the high-frequency content of small events will be filtered out lowering the S/N ratio and limiting the ability to derive source parameters. The used acquisition system must allow for covering the expected frequency band of the target earthquakes. This is especially important for analyses involving reliable estimation of static (seismic moment, corner frequency) and dynamic (radiated energy) source properties [*Baig and Urbancic*, 2010; *Viegas et al.*, 2012].

If the monitoring conditions are not optimal with respect to the target magnitude/frequency range of (expected) earthquakes, the data will allow for reduced detection and may lead to errors and biases in the analysis of source properties. A simple example is the apparent breakdown of self-similarity of earthquake source processes for small earthquakes due to the limited upper frequency band or inappropriate corrections for attenuation [*Ide et al.*, 2003; *Kwiatek et al.*, 2011, 2014; *Abercrombie*, 2015; *Harrington et al.*, 2015]. The radiated energy and corner frequency estimates are especially affected, as they require recording of high frequencies. Ideally, the sensor should record reliably as broad a range of frequencies as possible. In an extreme case, to capture 90% of the seismic energy of a given event, the sampling rate should be at least 10 times higher than its corner frequency [*Ide et al.*, 2003]. For example, an event with $M_W = -2.0$ may have observed corner frequency of 500 Hz. Analysis of source properties of such events requires a frequency band up to 5000 Hz, which theoretically necessitates 10 kHz sampling rate! Also, depletion in the low-frequency

content (e.g., due to the use of short-period sensors) leads to reduced detection capabilities of the seismic network for large events. More importantly, ignoring the low-frequency depletion leads to underestimation of magnitudes [*Baig and Urbancic*, 2010]. The information in Figures 11 and 12 allows deducing the optimum frequency range of the acquisition system with respect to the targeted magnitude range of seismicity.

Another factor affecting the detection and analyses of source properties is the rupture directivity. The assumed SH source model accounts for the variability of the STF with the directionality of the observation angle, but it has no directivity due to radial symmetry of the rupture propagation. Directivity enhances the S/N ratios and corner frequencies of the *P* and *S* waves at observation points in the direction of rupture propagation and decreases them in the opposite direction. This may balance out overall for detection purposes, perhaps with somewhat reduced signal quality because of the azimuthal variations of amplitudes and frequency content, and it can lead to errors in derived stress drops if not accounted for [e.g., *Calderoni et al.*, 2012].

Our detection analysis was based on the average radiation from pure shear and pure tensile faults associated with various focal mechanisms and all observation points, rather than focusing on individual focal mechanisms (and source-receiver angles). This means that the presented results are representative for any fault, assuming the focal sphere is sufficiently covered by the seismic network. For pure shear and pure tensile sources, the *P* wave amplitude involving particular focal mechanism and observation angle may vary by a factor of approximately 2 (±6 dB) and 1.7 (±5 dB), respectively, compared to the presented results based on the average radiation pattern. A similar range of variations holds for the *S* waves. However, in the case of *P* waves it is overall more likely that for a given observation point and random focal mechanism the recorded amplitude will be lower than the average radiation coefficient (=0.52) due to existence of radiation nodes. This is opposite for *S* waves, where it is overall more likely to have slightly larger amplitudes for a particular observation point and random focal mechanism compared to the averaged radiation (0.63) used in this study. The faulting type (pure shear/tensile) does not affect significantly the *S* wave radiation, but it does affect the *P* wave radiation. The presented theoretical results suggest that detection of tensile seismic events using *P* waves would be easier than shear events (+12 dB in amplitude of *P* waves) due to the enhanced *P* radiation. This can be relevant primarily for detection of explosions, since only small tensile opening/closing components are expected for earthquakes. However, we note that resolving tensile components of earthquakes is still important for improved understanding of source processes [e.g., *Kwiatek and Ben-Zion*, 2013; *Boettcher et al.*, 2015; *Ross et al.*, 2015].

We considered source-receiver distances of up to 50 km. At these distances direct waves may be accompanied by refracted and surface phases, and in some locations also basin and trapped waves with amplified motion. In such cases the S/N ratios are generally expected to be higher leading to increase in detection limits at larger distances. In addition, near-field terms ignored in our simulations may enhance the S/N ratio at very short distances. On the other hand, some factors such as strong site effects or significant scattering may reduce the S/N ratio in some situations. We also note that S/N ratios in individual stations are relevant for the first stage of event detection and additional processing steps (e.g., association of signals at multiple stations and successful location) are needed to declare event detection. Nevertheless, the results presented in this paper may be considered overall conservative, especially in cases with good coverage of the focal sphere and situations with lower ambient noise levels (e.g., when using borehole sensors).

From Figures 9–12 it is evident that to capture $M_W < -3.0$, the monitoring networks must be located very close to earthquakes to suppress the effects of attenuation and geometrical spreading and preserve the high-frequency content of the waveforms. This must be combined with adjustments to the acquisition system to handle high frequencies enabling the detection and reliable analysis of source properties. At a certain frequency this requires a change from standard seismic sensors to acoustic emission monitoring systems. For example, *Plenkers et al.* [2011] and *Kwiatek et al.* [2011] analyzed nanoseismicity and picoseismicity catalog of seismic events with M_W ranging from -5.0 to -1.0, recorded in Mponeng deep gold mine, South Africa. They found that to capture $M_W - 4.0$ earthquakes with seismic source of centimeter size and corner frequencies of up to 10 kHz [*Kwiatek et al.*, 2011] sensors must be closer than 100 m from the hypocenters, while detection of $M_W - 5.0$ events requires source-receiver distances no more than a few tens of meters. The actual required distance for such small events also depends strongly on sites effects, e.g., in the Mponeng deep gold mine location of fracture zones or tunnels [*Plenkers et al.*, 2009, 2010].

It is somehow intuitive to assume that it is easier to detect earthquakes using S waves rather than P phases, due to the fact that radiated energy of S waves is typically larger than that of P waves. In the case of the SH source model used here, the S/N ratio of S phases is approximately 10 times (+20 dB) higher than that of P phases when the path and sensor effects are neglected. However, different attenuation coefficients for P and S waves between the source and receiver can modify the relative S/N ratio of the waves, with high frequencies being most seriously affected. When the quality factors of P and S waves are comparable, the S amplitudes are always higher than the P amplitudes for the same set of source characteristics, regardless of magnitude. However, for the classical relation $Q_S = 4/9\ Q_P$ and small events generating high frequencies, the amplitude of S waves is lower than that of P wave beyond some propagation distance (Figure 13). The situation may be more complex in cases of frequency-dependent attenuation not considered in this work. The observed relative depletion in S wave amplitude relative to that of P waves with increasing distance and decreasing magnitude should be considered if using detection strategies based only on S waves. The examples shown illustrate that it is important to attempt detection using both P and S waves, especially for small events.

5. Conclusions

Our analysis of waveform properties of earthquakes with M_W between -3.0 and 5.0, corresponding to source corner frequencies between 7 kHz and 0.5 Hz and source sizes between 1 dm and 1 km, lead to the following conclusions:

1. For typical values of static stress drops (0.1–10 MPa) and rupture velocities (0.5–0.9 V_S), and all focal mechanisms, faulting types and observation points, the maximum amplitudes of the STF derivative (proportional to the far-field ground velocity) vary between -23 dB and $+14$ dB with respect to a source with $V_R = 0.9\ V_S$ and $\Delta\sigma = 1$ MPa (referred to as standard source in this work). The P wave amplitudes of a pure tensile source may be enhanced by $+12$ dB.
2. The amplitude and frequency content of seismic waveforms are primarily affected by the earthquake magnitude and static stress drop. Higher magnitudes generate higher ground motions; lower magnitudes generate higher-frequency waves, and larger stress drops (for a given magnitude) generate higher ground motions and frequencies. The rupture velocity, radiation pattern, and faulting type (shear/tensile) have secondary effects on the waveforms, which are not essential for considerations of earthquake detection but may be important for analyses of source properties.
3. The geometrical spreading and intrinsic attenuation produce clear limits to both detectability of events and analyses of earthquake source properties.
4. The S amplitudes generated by earthquake sources are always larger than the P amplitudes. However, stronger attenuation of S waves can lead to significant decrease of the S/P amplitude ratio for small events, and in some cases even produce P amplitudes larger than those of the S waves.
5. Inappropriate frequency band of the sensor and/or sampling frequency of the acquisition system can seriously affect the detectability and ability to analyze source properties of both small and large earthquakes.

References

Abercrombie, R. E. (2015), Investigating uncertainties in empirical Green's function analysis of earthquake source parameters, *J. Geophys. Res. Solid Earth*, *120*, 4263–4277, doi:10.1002/2015JB011984.

Allam, A. A., Y. Ben-Zion, I. Kurzon, and F. Vernon (2014), Seismic velocity structure in the Hot Springs and Trifurcation areas of the San Jacinto fault zone, California, from double-difference tomography, *Geophys. J. Int.*, *198*(2), 978–999, doi:10.1093/gji/ggu176.

Andrews, D. J. (1986), Objective determination of source parameters and similarity of earthquakes of different size, in *Earthquakes Source Mechanics*, vol. 37, edited by S. Das, J. Boatwright, and C. H. Scholz, pp. 259–267, AGU, Washington, D. C.

Baig, A., and T. Urbancic (2010), Magnitude determination, event detectability, and assessing the effectiveness of microseismic monitoring programs in petroleum applications *CSEG Rec.-Focus Artic.*, (February), 23–27.

Ben-Zion, Y. (2003), Appendix 2. Key formulas in earthquake seismology, in *International Geophysics*, vol. 81, Part B, edited by H. K. William et al., pp. 1857–1875, Academic Press, Boston, Mass.

Ben-Zion, Y., and J.-P. Ampuero (2009), Seismic radiation from regions sustaining material damage, *Geophys. J. Int.*, *178*, 1351–1356, doi:10.1111/j.1365-246X.2009.04285.x.

Ben-Zion, Y., F. L. Vernon, Y. Ozakin, D. Zigone, Z. E. Ross, H. Meng, M. White, J. Reyes, D. Hollis, and M. Barklage (2015), Basic data features and results from a spatially dense seismic array on the San Jacinto fault zone, *Geophys. J. Int.*, *202*(1), 370–380, doi:10.1093/gji/ggv142.

Boettcher, M. S., D. L. Kane, A. McGarr, M. J. S. Johnston, and Z. Reches (2015), Moment tensors and other source parameters of mining-induced earthquakes in TauTona Mine, South Africa, *Bull. Seismol. Soc. Am.*, *105*(3), 1576–1593.

Boore, D. M., and J. Boatwright (1984), Average body-wave correction coefficients, *Bull. Seismol. Soc. Am.*, *74*, 1615–1621.

Bouchon, M., V. Durand, D. Marsan, H. Karabulut, and J. Schmittbuhl (2013), The long precursory phase of most large interplate earthquakes, *Nat. Geosci.*, *6*(4), 299–302.

Brune, J. N. (1970), Tectonic stress and spectra of seismic shear waves from earthquakes, *J. Geophys. Res.*, *78*, 4997–5009, doi:10.1029/JB075i026p04997.

Brune, J. N. (1971), Correction, *J. Geophys. Res.*, *76*, 5002, doi:10.1029/JB076i020p05002.

Burdick, L. J. (1978), *t** for *S* waves with a continental ray path, *Bull. Seismol. Soc. Am.*, *68*(4), 1013–1030.

Calderoni, G., A. Rovelli, and S. K. Singh (2012), Stress drop and source scaling of the 2009 April L'Aquila earthquakes, *Geophys. J. Int.*, doi:10.1093/gji/ggs011.

Di Bona, M., and A. Rovelli (1988), Effects of the bandwidth limitation of stress drops estimated from integrals of the ground motion, *Bull. Seismol. Soc. Am.*, *78*(5), 1818–1825.

Dieterich, J. H. (1992), Earthquake nucleation on faults with rate- and state-dependent strength, *Tectonophysics*, *211*, 115–134.

Eshelby, J. D. (1957), The determination of the elastic field of an ellipsoidal inclusion, and related problems, *Proc. R. Soc. Lond. Ser. Math. Phys. Sci.*, *241*(1226), 376–396, doi:10.1098/rspa.1957.0133.

Futterman, W. I. (1962), Dispersive body waves, *J. Geophys. Res.*, *67*(13), 5279–5291, doi:10.1029/JZ067i013p05279.

Gibbons, S. J., and F. Ringdal (2006), The detection of low magnitude seismic events using array-based waveform correlation, *Geophys. J. Int.*, *165*(1), 149–166, doi:10.1111/j.1365-246X.2006.02865.x.

Gomberg, J. (1991), Seismicity and detection/location threshold in the Southern Great Basin Seismic Network, *J. Geophys. Res.*, *96*(B10), 16,401–16,414, doi:10.1029/91JB01593.

Harrington, R. M., G. Kwiatek, and S. M. Moran (2015), Self-similar rupture implied by scaling properties of volcanic earthquakes occurring during the 2004–2008 eruption of Mount St. Helens, Washington, *J. Geophys. Res. Solid Earth*, *120*, 4966–4982, doi:10.1002/2014JB011744.

Haskell, N. A. (1964), Total energy and energy density of elastic wave radiation from propagating faults, *Bull Seismol. Soc Am*, *54*, 1811–1841.

Hauksson, E., and P. M. Shearer (2006), Attenuation models (Q_P and Q_S) in three dimensions of the southern California crust: Inferred fluid saturation at seismogenic depths, *J. Geophys. Res.*, *111*, B05302, doi:10.1029/2005JB003947.

Hauksson, E., W. Yang, and P. M. Shearer (2012), Waveform relocated earthquake catalog for southern California (1981 to June 2011), *Bull. Seismol. Soc. Am.*, *102*(5), 2239–2244, doi:10.1785/0120120010.

Ide, S., G. C. Beroza, S. G. Prejean, and W. L. Ellsworth (2003), Apparent break in earthquake scaling due to path and site effects on deep borehole recordings, *J. Geophys. Res.*, *108*(B5), 2271, doi:10.1029/2001JB001617.

Inbal, A., R. W. Clayton, and J.-P. Ampuero (2015), Imaging widespread seismicity at midlower crustal depths beneath Long Beach, CA, with a dense seismic array: Evidence for a depth-dependent earthquake size distribution, *Geophys. Res. Lett.*, *42*, 6314–6323, doi:10.1002/2015GL064942.

Kaneko, Y., and P. M. Shearer (2015), Variability of seismic source spectra, estimated stress drop, and radiated energy, derived from cohesive-zone models of symmetrical and asymmetrical circular and elliptical ruptures, *J. Geophys. Res. Solid Earth*, *120*, 1053–1079, doi:10.1002/2014JB011642.

Knopoff, L. (1964), Q, *Rev. Geophys.*, *2*(4), 625–660, doi:10.1029/RG002i004p00625.

Kværna, T., F. Ringdal, J. Schweitzer, and L. Taylor (2002), Optimized seismic threshold monitoring—Part 1: Regional processing, *Pure Appl. Geophys.*, *159*(5), 969–987, doi:10.1007/s00024-002-8668-0.

Kwiatek, G., and Y. Ben-Zion (2013), Assessment of *P* and *S* wave energy radiated from very small shear-tensile seismic events in a deep South African mine, *J. Geophys. Res. Solid Earth*, *118*, 3630–3641, doi:10.1002/jgrb.50274.

Kwiatek, G., M. Bohnhoff, G. Dresen, A. Schulze, T. Schulte, G. Zimmermann, and E. Huenges (2010), Microseismicity induced during fluid-injection: A case study from the geothermal site at Gross Schoenebeck, North German Basin, *Acta Geophys.*, *58*(6), 995–1020, doi:10.2478/s11600-010-0032-7.

Kwiatek, G., K. Plenkers, and G. Dresen (2011), Source parameters of picoseismicity recorded at Mponeng Deep Gold Mine, South Africa: Implications for scaling relations, *Bull. Seismol. Soc. Am.*, *101*(6), 2592–2608, doi:10.1785/0120110094.

Kwiatek, G., F. Bulut, M. Bohnhoff, and G. Dresen (2014), High-resolution analysis of seismicity induced at Berlín geothermal field, El Salvador, *Geothermics*, *52*, 98–111, doi:10.1016/j.geothermics.2013.09.008.

Kwiatek, G., P. Martínez-Garzón, G. Dresen, M. Bohnhoff, H. Sone, and C. Hartline (2015), Effects of long-term fluid injection on induced seismicity parameters and maximum magnitude in northwestern part of The Geysers geothermal field, *J. Geophys. Res. Solid Earth*, *120*, 7085–7101, doi:10.1002/2015JB012362.

Lin, F.-C., D. Li, R. W. Clayton, and D. Hollis (2013), High-resolution 3D shallow crustal structure in Long Beach, California: Application of ambient noise tomography on a dense seismic array, *Geophysics*, *78*(4), Q45–Q56, doi:10.1190/geo2012-0453.1.

Madariaga, R. (1976), Dynamics of an expanding circular fault, *Bull. Seismol. Soc. Am.*, *66*, 639–666.

McGarr, A. (1991), Observations constraining near-source ground motion estimated from locally recorded seismograms, *J. Geophys. Res.*, *96*, 16,495–16,508, doi:10.1029/91JB01379.

McGarr, A., and J. B. Fletcher (2002), Mapping apparent stress and energy radiation over fault zones of major earthquakes, *Bull. Seismol. Soc. Am.*, *92*(5), 1633–1646, doi:10.1785/0120010129.

Moeck, I., G. Kwiatek, and G. Zimmermann (2009), Slip tendency analysis, fault reactivation potential and induced seismicity in a deep geothermal reservoir, *J. Struct. Geol.*, *31*(10), 1174–1182, doi:10.1016/j.jsg.2009.06.012.

Okada, Y., K. Kasahara, S. Hori, K. Obara, S. Sekiguchi, H. Fujiwara, and A. Yamamoto (2004), Recent progress of seismic observation networks in Japan—Hi-net, F-net, K-NET and KiK-net—, *Earth Planets Space*, *56*(8), 15–28, doi:10.1186/BF03353076.

Olsen, K. B., S. M. Day, and C. R. Bradley (2003), Estimation of *Q* for long-period (>2 sec) waves in the Los Angeles Basin, *Bull. Seismol. Soc. Am.*, *93*(2), 627–638, doi:10.1785/0120020135.

Orlecka-Sikora, B., E. E. Papadimitriou, and G. Kwiatek (2009), Study of the interaction among mining induced seismic events in the Legnica-Głogów Copper District, Poland, *Acta Geophys.*, *57*(2), 413–434, doi:10.2478/s11600-008-0085-z.

Ou, G. B. (2008), Seismological studies for tensile faults, *Terr. Atmos. Ocean Sci.*, *19*(5), 463–471, doi:10.3319/TAO.2008.19.5.463(T)1.

Peterson, J. (1993), Observation and modelling of seismic background noise, U.S. Geol. Surv. Tech. Rept.

Plenkers, K., G. Kwiatek, M. Naoi, and J. W. Group (2009), JAGUARS project: Attenuation, scattering and instrumental effects of events recorded by a high-frequency seismic network as seen from seismograms and their frequency content, in *Proceedings of the IASPEI General Assembly*, Cape Town, Republic of South Africa, 10–16 January 2009.

Plenkers, K., G. Kwiatek, M. Nakatani, G. Dresen, and J. Group (2010), Observation of seismic events with frequencies *f* > 25 kHz at Mponeng Deep Gold Mine, South Africa, *Seismol. Res. Lett.*, *81*(3), 467–478, doi:10.1785/gssrl.81.3.467.

Plenkers, K., D. Schorlemmer, and G. Kwiatek (2011), On the probability of detecting picoseismicity, *Bull. Seismol. Soc. Am.*, *101*(6), 2579–2591, doi:10.1785/0120110017.

Ross, Z., Y. Ben-Zion, and L. Zhu (2015), Isotropic source terms of San Jacinto fault zone earthquakes based on waveform inversions with a generalized CAP method, *J. Geophys. Res. Solid Earth*, *200*, 1269–1280, doi:10.1093/gji/ggu460.

Sato, T. (1978), A note on body-wave radiation from expanding tension crack, *Sci Rep Tohoku Univ*, *Ser. 5, Geophysics*, *25*, 1–10.

Sato, T., and T. Hirasawa (1973), Body wave spectra from propagating shear cracks, *J. Phys. Earth*, *21*, 415–432.

Shelly, D. R., G. C. Beroza, and S. Ide (2007), Non-volcanic tremor and low-frequency earthquake swarms, *Nature*, *446*(7133), 305–307, doi:10.1038/nature05666.

Snoke, J. A. (1987), Stable determination of (Brune) stress drops, *Bull Seismol. Soc Am*, *77*, 530–538.

Vavryčuk, V. (2001), Inversion for parameters of tensile earthquakes, *J. Geophys. Res.*, *106*(B8), 16,339–16,355, doi:10.1029/2001JB000372.

Venkataraman, A., and H. Kanamori (2004), Effect of directivity on estimates of radiated seismic energy, *J. Geophys. Res.*, *109*, B04301, doi:10.1029/2003JB002548.

Viegas, G., A. Baig, W. Coulter, and T. Urbancic (2012), Effective monitoring of reservoir-induced seismicity utilizing integrated surface and downhole seismic networks, *First Break*, *30*(7), 77–81.

Wu, C., Z. Peng, X. Meng, and Y. Ben-Zion (2014), Lack of spatio-temporal localization of foreshocks before the 1999 *Mw*7.1 Duzce, Turkey earthquake, *Bull. Seismol. Soc. Am.*, *104*, 560–566, doi:10.1785/0120130140.

Yang, W., and Y. Ben-Zion (2016), Corner frequency ratios of *P* and *S* waves and strain drops of earthquakes recorded by a tight network around the Karadere segment of the North Anatolian Fault Zone: Evidence for non-classical source processes, *Geophys. J. Int.*, *205*, 220–235, doi:10.1093/gji/ggv560.

Zigone, D., Y. Ben-Zion, M. Campillo, and P. Roux (2015), Seismic tomography of the southern California plate boundary region from noise-based Rayleigh and Love waves, *Pure Appl. Geophys.*, *172*(5), 1007–1032, doi:10.1007/s00024-014-0872-1.